atmosphere

MDPI

Article

Decadal changes in the Antarctic sea ice response to the changing ENSO in the last four decades

Young-Kwon Lim [1,3*], Dong L. Wu [2], Kyu-Myong Kim [2] and Jae N. Lee [2,3]

[1] Global Modeling and Assimilation Office (GMAO), NASA Goddard Space Flight Center, Greenbelt, Maryland, USA
[2] Climate and Radiation Laboratory, NASA Goddard Space Flight Center, Greenbelt, Maryland, USA
[3] University of Maryland, Baltimore County, Baltimore, Maryland, USA
* Correspondence: Young-Kwon.Lim@nasa.gov

Abstract: Sea ice fraction (SIF) over the Ross/Amundsen/Bellingshausen Sea (RAB) are investigated using the Modern-Era Retrospective Analysis for Research and Application, Version 2 (MERRA-2) focusing on the differences in time-lagged response to ENSO between the late 20th (1980-2000, L20) and the early 21st century (2001-2021, E21). Findings suggest that the typical Antarctic response to ENSO is influenced by changes in ENSO type/intensity, highlighting the need for caution when investigating the Antarctic teleconnection. Time-lagged regressions onto the mature phase of El Niño reveal that the SIF decrease and SST increase over the RAB is relatively weaker in E21 and most pronounced at 0-4 months lag. Conversely, the SIF in L20 continues to decline and reaches its peak at two-season lag (5-7 month). Tropospheric wind, pressure, and wave activity in response to El Niño in L20 show a zonally oriented high-/low-pressure areas with two-season lag, enhancing the poleward flow that plays a key role in sea ice melt in the RAB, while this pattern in E21 is insignificant at the same lag. This study suggests that stronger (weaker) and more eastern (central) Pacific ENSOs on average in L20 (E21) are associated with this decadal change in the SIF response to ENSO.

Keywords: Antarctic sea ice; Antarctic Dipole; climate variability; Ross; Amundsen; Weddell; ENSO

Citation: To be added by editorial staff during production.

Academic Editor: Firstname Lastname

Received: date
Revised: date
Accepted: date
Published: date

1. Introduction

Teleconnection in the Antarctic as a remote response to ENSO

The El Niño-Southern Oscillation (ENSO) has a significant impact on Antarctic climate variability, particularly on interannual sea ice variations across the Ross, Amundsen, Bellingshausen (referred to as RAB for the three Seas) and Weddell Sea [1-8]. This influence is attributed to a large-scale teleconnection called the Pacific South American (PSA) pattern [9-15], which is considered the strongest Antarctic teleconnection to ENSO on an interannual time scale [4, 11, 16-18]. The PSA pattern is generated by tropical Pacific sea surface temperature (SST) anomalies developed by the ENSO effect, acting as a heat source that generates Rossby wave propagation across the Southern Ocean (SO), spanning the Antarctic region [19-25]. The subtropical jet acts as a waveguide for this Rossby wave train to link the tropical ENSO forcing to high latitude atmospheric processes [18, 20]. The circulation and pressure systems associated with the PSA result in opposite sea ice anomalies between the RAB and the Weddell Sea [13, 15, 18, 26], creating the Antarctic dipole (AD) structure: sea ice decrease (increase) over the RAB (Weddell) during El Niño, and the opposite during La Niña.

Impact of ENSO type and intensity change on the Antarctic teleconnection

Earlier investigations based on late 20th-century data suggest that the impact of the PSA pattern on sea ice anomalies across the RAB and Weddell Sea persists 3-4 seasons after the mature phase of ENSO [18]. Due to the limited number of ENSO samples available from that period, it raises questions about the robustness of the conclusion when considering the longer-term changes (e.g., decadal time scale) in the dominant types and intensities of ENSO. Climate change may also alter the spatiotemporal evolution of the PSA and AD teleconnections to ENSO [27-29]. Recent studies indicate that the properties of ENSO have been evolving over the recent past decades [30, 31]. For instance, Yu et al., Yeo and Kim, and Zhang et al. [31-33] identify more occurrence of the EP type ENSO during the late 20th century (L20), while CP type ENSO events have become more prevalent in the early 21st century (E21). Furthermore, studies have observed significant decadal changes in the horizontal distribution of Rossby wave propagation towards the Southern Ocean over the past several decades [26, 32]. This has implications for the way ENSO influences the climate patterns in the Antarctic region.

Previous research highlighted that the variability of Antarctic sea ice responses may depend on the type of El Niño, specifically distinguishing between eastern Pacific (EP) and central Pacific (CP) El Niño events [34, 35]. Zhang et al. [33] reveals that EP El Niño events generate tropical heat sources that excite a Rossby wave train propagating in a different direction compared to CP El Niño events. Chen et al. [36] also found that this Rossby wave train during CP El Niño is weak and westward-shifted, relative to EP El Niño. As a result, the circulation patterns and locations of sea ice retreat or advance across the RAB and Weddell Sea differ between EP and CP El Niño events, with the sea ice melt region approximately 20° east of that seen in CP El Niño [33]. Yu et al. [31] concludes that, while the EP ENSO can excite only the PSA, the CP ENSO can excite both the Southern Annular Mode (SAM) [37, 38] and PSA, with frequent in-phase relationship of those two modes and strengthened AD pattern. It's worth noting, however, that these conclusions from Yu et al. [31] and Zhang et al. [33] were drawn specifically for the Austral spring period (September to November) during ENSO development years. The characteristics of wave propagation and sea ice response may vary in different seasons and during different ENSO phases, such as developing and decaying phases. In Song et al. [39], the CP ENSO is shown to change the regional Pacific Ferrel cells of Southern Hemisphere more efficiently, leading to a prolonged duration of the AD pattern compared to the scenario with EP ENSO. However, Dou and Zhang [26] proposed that, when focusing on the austral cold season that follows ENSO maturity, the correlation between the AD pattern and ENSO gets weaker in recent decades, particularly during periods of more frequent CP ENSO occurrences. Likewise, the conclusions drawn on the relationship between the ENSO type and the Antarctic sea ice appear to be varied among earlier studies.

Not only the type of ENSO, but also the intensity of ENSO seems to have undergone decadal change over the last four decades. However, there has been very limited research on the Antarctic teleconnection variation between two decadal-scale periods with different ENSO intensities, in contrast to the extensive investigation into the impact of two distinct ENSO types. Our examination in Section 3.3 indicates that, on average, ENSO is less intense in the E21 period than in the L20 period by more than 30% based on the amplitude of the Niño3.4 SST anomaly. We anticipate that this decadal difference in ENSO intensity also influences the teleconnection between the tropical Pacific and Antarctica, resulting in distinct changes in atmospheric circulation, AD pattern, and the response of sea ice.

Motivation and expected contribution of this study to the Antarctic climate science

This study is motivated by the existing unresolved questions surrounding the way sea surface temperature (SST)/sea ice respond to changing ENSO over the last four decades. Notably, the long-term alteration in the AD pattern in conjunction with the ENSO variations has still to be more thoroughly investigated, considering both the type and intensity shifts in ENSO. Our study proposes that this decadal shift in the AD pattern contributes to an increase in the amplitude of annual mean sea ice anomaly with time in the Antarctica as we elucidate in Section 3.1. There is also a need for further demonstration regarding the specific time-lag at which sea ice anomalies over the RAB and Weddell Sea reach their peak in response to different nature of ENSO events. This study primarily focuses on how the matured phase of ENSO influences Antarctic climate over the subsequent three seasons within two different periods: L20 and E21. We expect that advance in understanding of these responses and the role of different atmospheric variables involved would help to gain a more complete picture of the relationship between ENSO and Antarctic sea ice response.

The paper is organized as follows. Section 2 introduces observation data, reanalysis products, and methodology utilized in this study. Section 3 explores the decadal change in the response of sea ice and SST to the changing ENSO in the last four decades. Section 4 provides discussion about the cause of this decadal change in ENSO and sea ice response. It also outlines the research plans for the future. Section 5 then presents the concluding remarks.

Table 1. List of abbreviation used in this study

RAB	**Ross/Amundsen/Bellingshausen**	**SO**	**Southern Ocean**
SIF	**Sea ice fraction**	**EP**	**Eastern Pacific**
PSA	**Pacific South American**	**CP**	**Central Pacific**
SAM	**Southern Annular Mode**	**L20**	**Late 20th century**
AD	**Antarctic Dipole**	**E21**	**Early 21st century**

2. Data and Method

2.1. Data

Observation and reanalysis data are used over the period from January 1980 to November 2022 in this study. The observed SST is obtained from the Merged Hadley-NOAA/OI SST [40]. Monthly Niño3.4 SST anomaly time series provided by NOAA Climate Prediction Center (CPC) is used as an ENSO index to compute the moving correlations between the ENSO and SST over the RAB. Reanalysis variables for analysis are obtained from the Modern-Era Retrospective analysis for Research and Applications, Version 2 (MERRA-2) [41]. The variables used are upper-tropospheric geopotential height, temperature, zonal and meridional wind at 300 hPa, vertical wind at each pressure level from 1000 hPa to 100 hPa, and sea level pressure (SLP) [42], near-surface wind at 2 m level [43], and sea ice fraction [44]. While there are acknowledged limitations in reanalysis sea ice, the MERRA-2 model effectively portrays various surface hydrological processes such as surface albedo, meltwater runoff, snow dynamics, and refreezing. Additionally, the MERRA-2 model bases its sea ice concentration boundary conditions on presently accessible high-resolution daily products [41]. Furthermore, this study finds that the atmospheric circulation and teleconnection align more accurately with MERRA-2 sea ice dynamics, indicating a better dynamic balance. To validate the MERRA-2 sea ice data, certain findings such as interannual time series (Figure 1a in Section 3.1) and regressed patterns derived from the MERRA-2 sea ice (Figure 5 in Section 3.4) were confirmed using sea ice extent from the National Snow and Ice Data Center (NSIDC) [45] and another reanalysis sea ice from the fifth generation ECMWF atmospheric reanalysis (ERA5) [46] employed in previous studies [47] (see appendix Figures 1 and 2).

2.2. Method

To better understand the temporal changes and their casual relationships among sea ice, SST, lower- and upper-level circulation, and wave activity fluxes in response to tropical ENSO forcing, we employ time-lagged moving correlation and regression as the primary approaches.

First, the SST and SIF time series are detrended using the least square estimate to eliminate any trend-related influence on correlations. Moving correlations are then calculated between SIFs in the RAB and the Weddell Sea area over 1980-2021 period applying a sliding window spanning 21 years to clearly represent the significant decadal change in SIF relationship between those two regions. Time-lagged moving correlations are also calculated between Niño3.4 SST at ENSO maturity (averaged for December, January, and February) and RAB SST/SIF in subsequent months to illustrate the changes in their time-lagged relationship from the L20 to E21 periods. The Pearson correlation method is employed to compute these correlations. To determine the significance of the results, a critical value of the correlation at 95% confidence is calculated based on the t-test with N-2 degrees of freedom, where N represents the sample size.

Second, the anomaly time series of sea ice, SST, lower- and upper-level circulation, and wave activity fluxes (WAF) are regressed at each grid point, with time-lags up to 11 months, against the mature phase of ENSO represented by Niño 3.4 SST anomaly in the boreal winter. This regression is also applied to vertical wind anomalies over the central/eastern Pacific sector from 1000hPa to 100hPa levels to reveal their vertical structure, such as the Hadley/Ferrell cell from the tropics through the Antarctic connected with the boreal winter ENSO. The significance of the regressed anomalies is tested using a two-tailed t-test.

The purpose of calculating WAF vectors is to assess how large-scale waves propagate spatially toward Antarctica in response to the ENSO. The WAF is an useful tool for presenting a snapshot of stationary or migratory quasi-geostrophic wave propagation and also helps inferring the origin of the waves [48]. Following Plumb [49], the expression for the stationary WAF is as follows

$$F_s = p\cos\varphi \begin{pmatrix} v'^2 - \frac{1}{2\omega\sin\varphi}\frac{\partial(v'\Phi')}{\partial\lambda} \\ -u'v' + \frac{1}{2\omega a\sin 2\varphi}\frac{\partial(u'\Phi')}{\partial\lambda} \\ \frac{2\omega\sin\varphi}{S}\left[v'T' - \frac{1}{2\omega a\sin 2\varphi}\frac{\partial(T'\Phi')}{\partial\lambda}\right] \end{pmatrix}$$

where the variables (u, v), p, T, and Φ represent the zonal and meridional wind, pressure, temperature, and geopotential height, respectively, and where λ and φ represent longitude and latitude. The constant ω corresponds to the Earth's rotation rate (=7.292×10^{-5} rad s^{-1}), and a is the radius of the earth. The prime symbol denotes the deviation from the zonal mean at each latitude and height for each month.

Furthermore, the Rossby wave source (RWS) [50] is calculated to distinctly pinpoint the origin of the wave. The linearized form of RWS derived from the quasi-geostrophic vorticity equation is

$$RWS = -V'_\chi \cdot \nabla(\bar{\zeta} + f) - (\bar{\zeta} + f)\nabla \cdot V'_\chi - \zeta'\nabla \cdot \bar{V}_\chi - \bar{V}_\chi \cdot \nabla\zeta'$$

where the climatological mean is indicated by the overbar, while the anomaly calculated from regression is represented by the prime symbol. On the right side of the equation, the first and fourth terms are related to vorticity advection, while the second and third terms are connected to the creation of wave vorticity through the divergence of the divergent wind, which is also known as vorticity stretching. Further detailed description of the RWS is available in Sardeshmukh and Hoskins [50]. Our calculation establishes that the tropical Pacific SST anomaly associated with ENSO occurrence serves as the primary source area for these waves propagating to the RAB, particularly during the mature phase of ENSO and the following boreal spring, as detailed in Section 4.2.

3. Results

3.1. Decadal change in the Antarctic Dipole (AD) pattern

The interannual variations of Antarctic sea ice over the last four decades is found to undergo notable changes from a negative correlation between the RAB and the Weddell Sea in L20 to a positive correlation in E21 in association with the weakening of the AD pattern. The time series of the annual mean sea ice extent across the entire Antarctic in Figure 1a shows a slight upward trend (indicating an increase in sea ice) until ~2015, followed by a decline. This mirrors a downward SST trend until ~2015, and a subsequent rise over Antarctica as discussed in earlier study [51]. More interestingly, the time series shows a growing amplitude of interannual variation over time. It raises interesting questions on whether this phenomenon is linked to the weakening of the AD pattern in the E21 period. In contrast to the L20 period, where the AD pattern generates organized opposing sea ice anomalies between RAB and Weddell Sea (Figure 1b), resulting in minimal averaged anomalies over these two seas, the E21 period lacks this opposing structure between the two regions (Figure 1b). Instead, the E21 period often displays sea ice anomalies with the same sign across the region, contributing to a relatively higher amplitude of sea ice anomaly as depicted in Figure 1a. Notably, the interannual variation of sea ice in Figure 1b is largely in phase with the variation in Figure 1a during the E21 period, highlighting that the variability of Antarctic sea ice is substantially influenced by the sea ice in the RAB and Weddell Sea regions. Our analysis reveals that approximately 73% of the year-to-year variation in Antarctic sea ice during the E21 period can be attributed to the sea ice in the RAB and Weddell Sea, as indicated by the standard deviation. A moving correlation of sea ice fraction between these two areas applying a 21-year sliding window in Figure 1c reveals a significant change in sign from negative to positive demonstrating a marked weakening of the AD pattern in the E21 period. This dramatic shift towards a positive correlation quite differs from the traditional perception of the connection between the sea ice anomaly in the RAB and Weddell Sea. This holds significance as it challenges the established understanding that the AD pattern, a prominent teleconnection pattern crucial for understanding sea ice anomalies, may not consistently and significantly account for the variations in sea ice in this region. This could be attributed to the changing influence of factor such as ENSO that governs the variability of the AD, as the shift in ENSO type/intensity from the L20 to E21 and associated atmospheric and sea ice change will be examined in detail in this study.

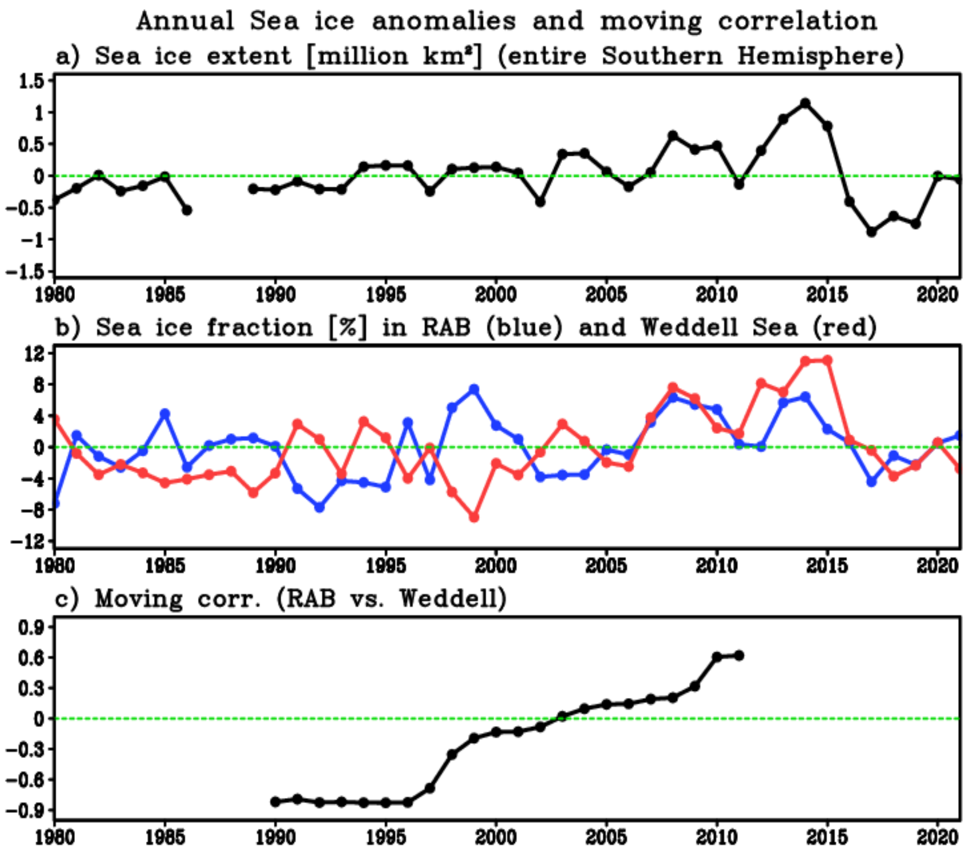

Figure 1. a) Time series of annual mean NSIDC sea ice extent anomaly (million km^2) averaged over the entire Southern Hemisphere. b) Time series of MERRA-2 sea ice fraction anomaly (%) for the Ross-Amundsen-Bellingshausen (RAB) Sea denoted by blue line and for the Weddell Sea denoted by red line. c) Moving correlations between the sea ice fraction from RAB and Weddell Sea shown in b). 21-year sliding window is applied to calculate the moving correlations. A significant change in correlation is evident when comparing the 20th century (with a negative correlation) to the 21st century (exhibiting a positive correlation). According to a t-test with N-2 degrees of freedom (where N equals 21), the critical correlation value at a 95% confidence level is approximately ±0.43.

The regression analysis of annual mean SST and 2-meter wind onto the SIF over the RAB and Weddell Sea in Figure 2 showcases distinct SST patterns in the two periods: opposing (same) anomalies over RAB and Weddell during the L20 (E21), reflecting a robust (diminished) AD structure. Interestingly, the SST pattern in the tropical Pacific resembles the distribution associated with ENSO. The pattern elucidates a decrease (increase) in SST with a concurrent rise (decline) in sea ice over RAB (Weddell) Sea during La Niña, and the reverse pattern during El Niño [18, 26]. This ENSO-related distribution is evidently prevalent in the L20 (Figures 2a,c), but considerably weaker in the E21 period (Figures 2b,d). Wind patterns at 2-meter level show equatorward flow over Ross and Amundsen regions and poleward flow over Bellingshausen and Weddell Sea during La Niña, with the opposite flow during El Niño. Based on the findings in Figures 1 and 2, we suggest that this substantial weakening of the AD pattern may be associated with the decadal-scale change in ENSO type and intensity, potentially inducing differing forms of sea ice response. Our subsequent focus involves an in-depth examination of atmospheric, SST, and sea ice responses to decadal change in ENSO, incorporating time-lagged responses and their decadal-scale changes.

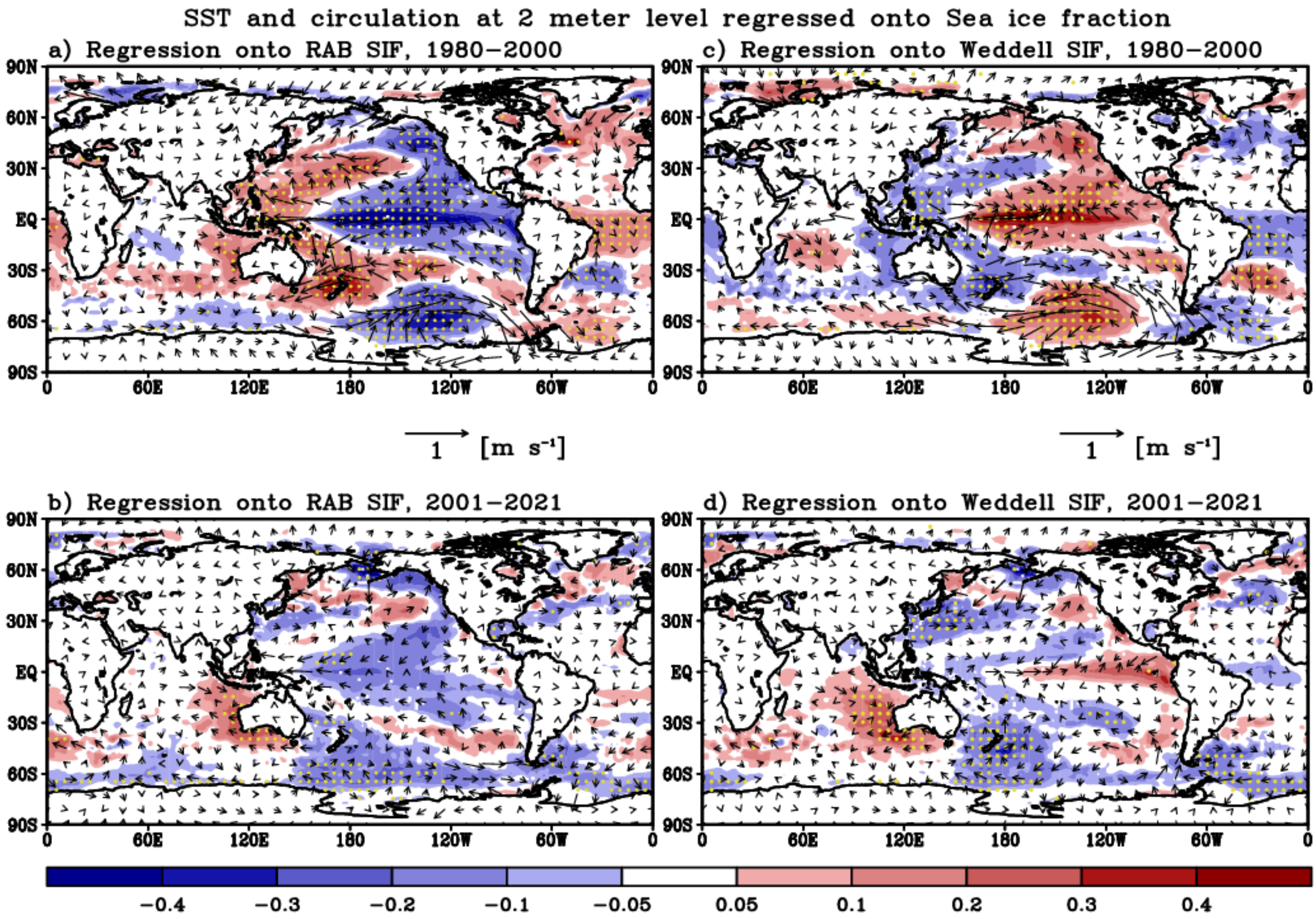

Figure 2. Annual mean anomalies of sea surface temperature (shaded) and horizontal wind vectors at 2-meter level [m s^{-1}] regressed onto the sea ice fraction over the Ross-Amundsen-Bellingshausen (RAB) Sea (left panel) and over the Weddell Sea (right panel). Upper panel (a,c) represents the result for the late 20th century (L20, 1980-2000) period, while lower panel (b,d) is the result for the early 21st century (E21, 2001-2021) period that has overall weaker regressed anomalies than the L20 period. Yellow stippled areas indicate that the anomalies are statistically significant at 95% confidence levels.

3.2. Decadal change in the relationship between the RAB SST/sea ice and ENSO

Time-lagged relationship between the mature phase of ENSO and RAB SST/sea ice in subsequent seasons is found to be more robust during the L20, with the ENSO influence persisting over a longer span, compared to the E21 period. To investigate the evolution of the connection between the mature phase of El Niño (specifically, boreal winter Niño3.4 SST) and the SST/sea ice over the RAB Sea across subsequent seasons, we employ time-lagged moving correlations over the last four decades, utilizing a sliding window spanning 21 years. Results are plotted for relatively shorter time lags of 1 to 4 months (denoted by red lines) and longer lags of 5 to 7 months (denoted by blue lines) in Figure 3. The results for 1-4 month lag interval reveal a consistent trend: during the L20 period, the SSTs exhibit strong correlations, characterized by correlation coefficients ranging from 0.5 to 0.8 (as depicted in Figure 3a). In contrast, this correlation in the E21 diminishes notably to 0.3 (depicted in Figure 3a). This substantial alteration in correlation, indicative of a decadal shift, is discernible across all considered time lags (ranging from 1 to 7 months).

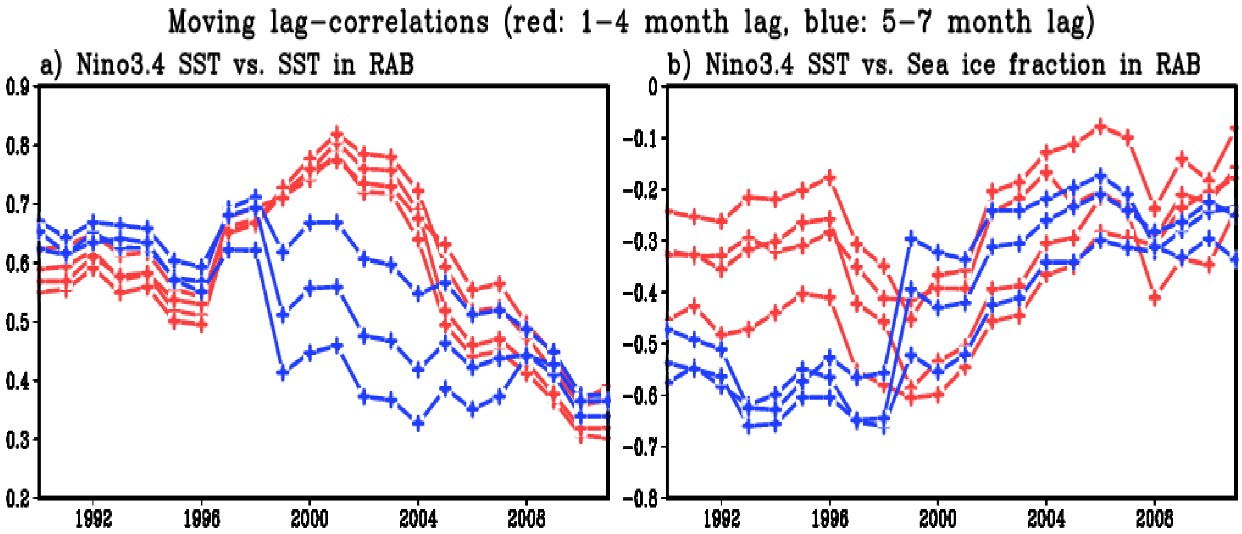

Figure 3. Time-lagged moving correlations over 1980-2021 period applying a sliding window spanning 21 years. The left panel (a) shows the correlations between the Niño3.4 SST and SST over the Ross-Amundsen-Bellingshausen (RAB) Sea while the SST over the RAB is switched to sea ice fraction in the right panel (b). Results are plotted in red lines for time lags of 1 to 4 months and blue lines for time lags of 5 to 7 months. The critical correlation value at a 95% confidence level, based on a t-test with N-2 degrees of freedom (where N equals 21), is approximately ±0.43. Positive relationship between the two SSTs in the left panel and negative relationship between the Niño3.4 SST and sea ice fraction in RAB is stronger in the late 20th century. Amplitude of correlations are also larger for longer time lag in the late 20th century, while that feature is not evident in the early 21st century.

Comparison in correlations between shorter lags (red lines) and longer lags (blue lines) indicates that until the sliding window centered around 1998, the correlations are notably stronger for longer lags, while that feature is no longer observable in the E21 period. This stronger correlation for longer lags in the L20 period is similarly apparent for sea ice, as depicted in Figure 3b. The negative correlation, denoting a decrease in sea ice during El Niño, is more pronounced for longer lags, and this strong connection to ENSO over extended lags is particularly evident during the L20 period. This divergence between the two lag intervals seems to indicate a more enduring and potent ENSO impact, associated with greater ENSO intensity during the L20 period (please refer to Table 2 and the next section for a comparison of ENSO intensity). Overall, Figure 3 underscores a more robust association between RAB SST/sea ice and ENSO, with the ENSO influence persisting over a longer span during the L20 period in contrast to the E21 period.

Table 2. List of ENSO years in the order of the amplitude of Niño 3.4 SST anomaly during mature phase for El Niño (second row) and La Niña (third row). ENSO years in the 20th century are in bold phase.

	ENSO years in the order of the amplitude of Niño 3.4 SST anomaly
El Niño	2015, **1997**, **1982**, **1991**, 2009, **1986**, **1994**, 2002, **1987**, 2018, 2004, 2006, 2014, 2019
La Niña	**1988, 1999**, 2007, **1998**, 2010, 2020, 2021, **1984**, **1995**, 2011, 2005, 2008, 2017, **1983**, 2000, 2016

3.3. Difference in the type and intensity of ENSO between the L20 and E21

An important question is why there is a significant decadal change in this correlation. In association with the possible role of ENSO in this correlation change, it is found that there is a notable change in type and intensity of ENSO from the L20 to E21 period. For example, the observational data on SST anomalies in the equatorial Pacific indicates that the EP type ENSO events are relatively more frequent during the L20 compared to the E21 [31-33]. The composite analysis of SST anomalies during ENSO events in Figure 4 clearly demonstrates that in the L20 period, the SST anomaly distribution extends prominently to the eastern equatorial Pacific, resembling the EP type ENSO pattern (Figures 4a,b). Conversely, the maximum amplitude of the SST anomaly in the E21 period is found in the central equatorial Pacific with a less pronounced extension towards the far eastern Pacific for both ENSO warm and cold events, similar to the CP type ENSO pattern (Figures 4c,d). Comparison in the SST variance between L20 and E21 period over Niño3 (150°W-90°W, 5°S-5°N) region to indicate decadal change in the EP type ENSO activity reveals 1.53 during L20 and 0.84 during E21. SST variance in the Niño4 (160°E-150°W, 5°S-5°N) region that represents the CP type ENSO activity is 0.67 in L20 and 0.79 in E21. These SST variances clearly indicate more active EP type ENSO during L20 whereas the CP type ENSO during E21.

The intensity of the ENSO, as indicated by the amplitude of the boreal winter Niño3.4 SST anomaly, is shown to be ~34% larger for El Niño (L20: 1.59°C vs. E21: 1.19° C) and ~53% larger for La Niña (L20: -1.31°C vs. E21: -0.85°C) in the L20, pointing to a higher frequency of strong ENSO events than in the E21. The interannual variability of the boreal winter Niño3.4 SST is also found to be larger in the L20, measuring 1.18, compared to 0.89 in the E21. Table 2 shows that out of a total 6 El Niño events that occurred in the L20, 5 of them are classified as stronger events, while the events in the E21 tend to be weaker, with an exception for the events in 2009 and 2015. In the case of La Niña events (the third row in Table 2), more weaker events were observed in the E21, along with three of the top four strongest events from the L20 period. The shift in ENSO type and intensity over decades holds great significance. It's crucial because the weakening of the AD in the E21 and the alteration in the sea ice pattern in the RAB and Weddell Sea are associated with this decadal shift in ENSO, as their connection is illustrated in Figure 2.

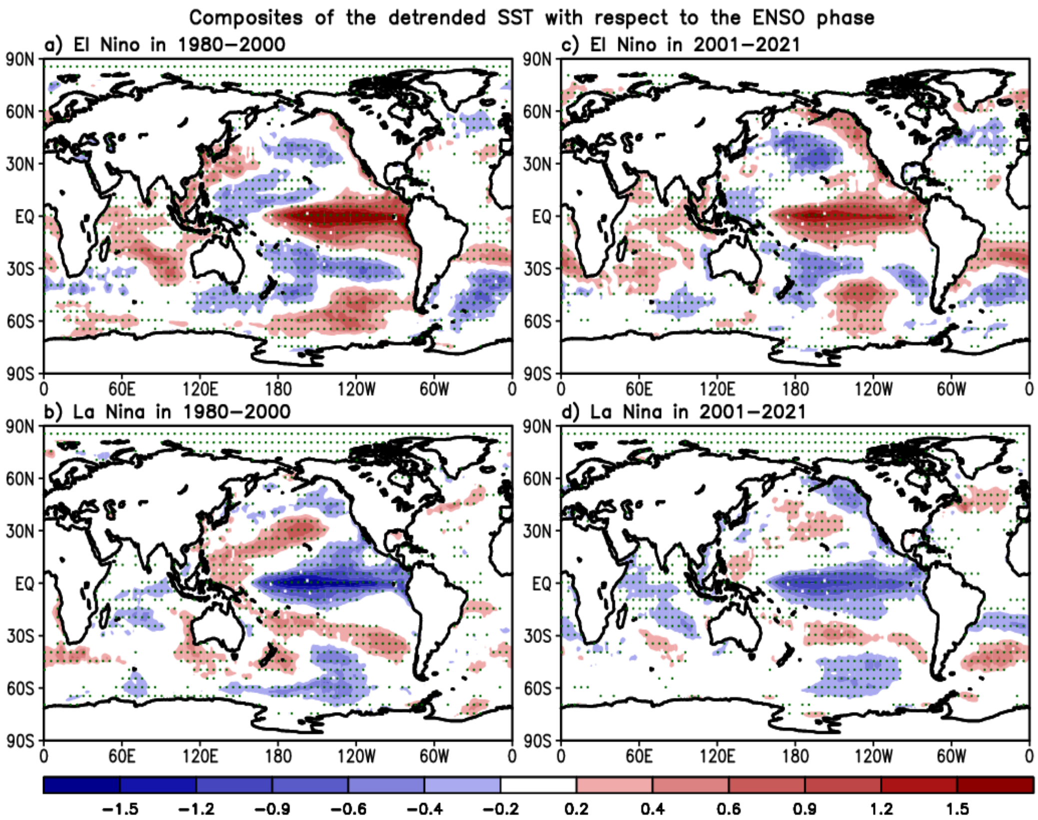

Figure 4. Composite of the detrended SST anomaly with respect to El Niño (upper panel, a and c) and La Niña (lower panel, b and d). The left panel (a,b) represents the result for the late 20th century while the right panel (c,d) is the result for the early 21st century period. The amplitude of anomaly in the tropical Pacific (ENSO occurrence region) is clearly larger for the late 20th century. Green stippled areas indicate that the anomalies are statistically significant at 95% confidence levels.

3.4. Lagged responses of the SST and sea ice to the mature phase of ENSO

Considering that the ENSO exhibits different characteristics in terms of type and intensity between the two analyzed periods, we explore whether the remote response of SST, sea ice, and circulation anomalies over the Antarctic region to tropical ENSO forcing also displays notable dissimilarities during these periods. Stronger connection of SST and sea ice with the ENSO, with ENSO impact on SST/sea ice persisting longer in subsequent months, is found during the L20 period. To identify meaningful decadal differences, we examine the regressed distributions. Figure 5 illustrates time-lagged regressed maps of the SST and sea ice fraction in response to the boreal winter Niño3.4 SST anomaly. Our primary focus is on the impact of ENSO maturity on the SST and sea ice variation in the subsequent three seasons, as previously noted in Section 1.

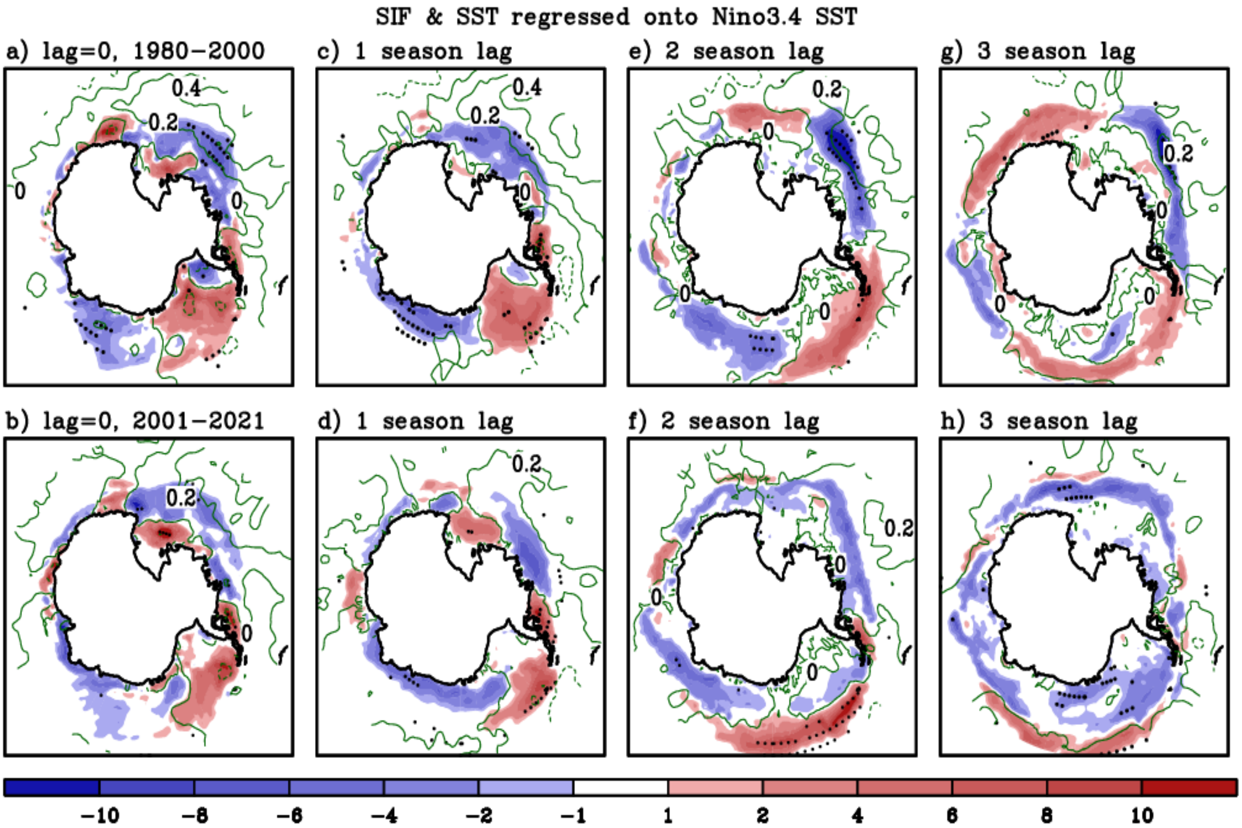

Figure 5. Distribution of SST (green contoured) and sea ice fraction (shaded) anomaly regressed onto the boreal winter Niño3.4 SST (averaged for December, January, and February). Each panel from the left to the right represents the regressed distributions considering 0, 1, 2, and 3 season lag. Results for the late 20th century are shown on the upper panel (a,c,e and g) while the lower panel (b,d,f and h) corresponds to the result for the early 21st century. The regressed anomaly over the Ross-Amundsen-Bellingshausen Sea reaches the maximum at 2 season lag in the late 20th century, while the amplitude gets weak at the same lag in the early 21st century. Black stippled areas indicate that the anomalies are statistically significant at 95% confidence levels.

The time evolution of the regressed patterns indicates a dominant sea ice decrease in the RAB Sea regions and an increase in the Weddell Sea from simultaneous to 2-season lag for both the L20 and E21 periods, representing a realistic typical PSA response to ENSO found in many earlier studies [4, 11, 16-18] (Figures 5a-f). This lagged response is still evident at the 3-season lag in the L20 (Figure 5g), but is not in the E21 period (Figure 5h). AD structure also persists through the 3-season lag in the L20, while the weakening of the AD pattern is seen with negative sign of anomalies over both the RAB and Weddell Sea starting at the 2-season lag in the E21 (Figures 5e-h). Another noteworthy difference in the sea ice distribution between the two periods is that the most substantial reduction in sea ice in the RAB Sea occurs at a 1-season lag (i.e., MAM) in the E21 period (Figure 5d). On the other hand, the L20 period continues to display a remarkable sea ice decrease, reaching its peak at a 2-season lag (i.e., JJA) (Figure 5e), suggesting that the impact of ENSO endures for a longer duration compared to the E21 period. Additionally, the area of the most significant sea ice reduction shifts eastward, closer to the Bellingshausen Sea, in the E21 period (Figures 5d,e). This indicates that the primary path of atmospheric wave propagation as a teleconnection to ENSO may differ between the L20 and E21 periods.

The regressed SST anomaly displayed in Figure 5 illustrates an increase (decrease) in SST in the RAB Sea region off the Antarctic coast due to the impact of El Niño (La Niña). This characteristic is evident in both periods (contours in Figure 5) and is closely related to the distribution of sea ice anomalies: sea ice tends to decrease (increase) in response to positive (negative) SST anomalies. However, a notably different feature in SST anomalies between the two periods is that the magnitude of the anomaly is larger in the RAB Sea during the L20, indicating a higher potential for causing more substantial sea ice melt (recovery) in response to El Niño (La Niña) compared to the E21 period. This distinction is evident as the contour line of the positive 0.2 anomaly is positioned closer to the Antarctic coast in the L20, while the same contour line is situated much farther from Antarctica in the E21.

Figure 6 clarifies that the response of sea ice to ENSO maturity is more pronounced and lasts longer over the RAB during the L20 period. The analysis involves counting the number of grid points for each sea ice fraction anomaly and time lag (ranging from 0 to 11 months) over the longitudes encompassing the RAB and Weddell Sea. Figure 6 clearly reveals that the largest sea ice decrease (mainly contributed by negative anomalies in the RAB Sea) occurs at a 5-7 month lag (indicated by red lines in Figure 6a). The magnitude of the negative anomaly on the x-axis indicates a SIF reduction greater than 10%. However, in the E21 period, the sea ice decrease appears to be strongest at shorter time-lags (0-4 months, blue lines), and most grid points exhibit an amplitude not exceeding 10% (Figure 6b). The distinctions between the two periods suggest a more pronounced impact of El Niño on reducing SIF over the RAB during the L20. On the other hand, the sea ice increase in response to El Niño (primarily found in the Weddell Sea) does not necessarily display the largest amplitude at a 5-7 month lag during the L20. In both periods, the most significant sea ice increase occurs at shorter time-lags (0-4 months).

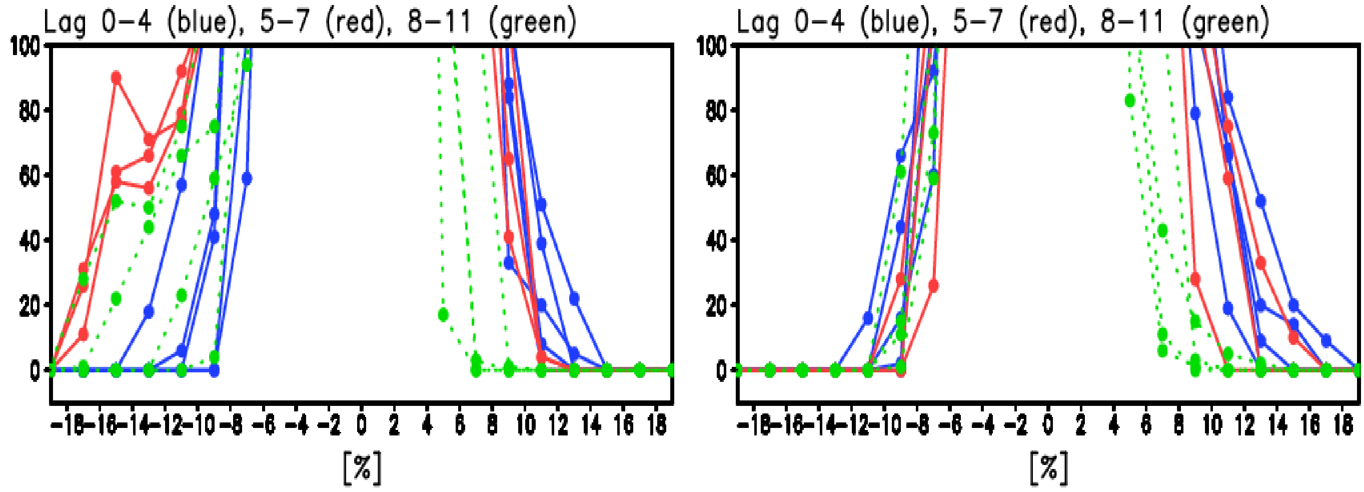

Figure 6. The number of grid points (y-axis) with respect to the regressed sea ice fraction (SIF) anomaly values (%, x-axis) distributed over the longitudes encompassing the Ross, Amundsen, Bellingshausen, and Weddell Sea. The regression is conducted onto the boreal winter Niño3.4 SST. Different colored lines (blue, red, and green) illustrate the outcomes for regressions at lags of 0-4 months, 5-7 months, and 8-11 months. In the left panel, the focus is on the late 20th century, while the right panel pertains to the early 21st century. The most significant decrease in SIF occurs at a lag of 5-7 months (indicated by the red lines) during the late 20th century (left panel).

4. Discussion

In this section, we discuss the possible reason for the decadal change in the sea ice response to ENSO, with a specific emphasis on the influence of circulation and pressure in both the lower and upper troposphere.

4.1. Lagged responses of the lower atmosphere to the mature phase of ENSO

Meridional component of the wind at lower atmosphere is found to behave quite differently in response to ENSO between the L20 and E21 period. To provide a detailed interpretation for the difference in the sea ice response over the RAB Sea region between the two periods, we examine the near-surface wind fields, considering their time-lagged response to the boreal winter Niño3.4 SST. Our focus is particularly on the meridional component of the 2-meter level wind to find out the evolution of equatorward/poleward wind flow, which can influence the RAB Sea by bringing colder or warmer air. The regressed 2-meter level meridional wind in Figure 7 reveals that during the L20 period, the poleward wind develops and reaches its maximum at approximately 150°W and 2-season lag (Figure 7e). This maximum poleward wind anomaly at these longitudes correlates well with the peak in sea ice decrease observed at a 5-7 month lag in the Ross and Amundsen Sea region. On the other hand, in the E21 period, the maximum poleward wind anomaly is located east of 120°W at a 1-season lag (Figure 7d), which is physically consistent with the largest sea ice decrease in this longitude, as shown in Figure 5. Zhang et al [33] also highlighted the significance of the meridional wind anomaly as a key factor in determining sea ice anomalies within this region.

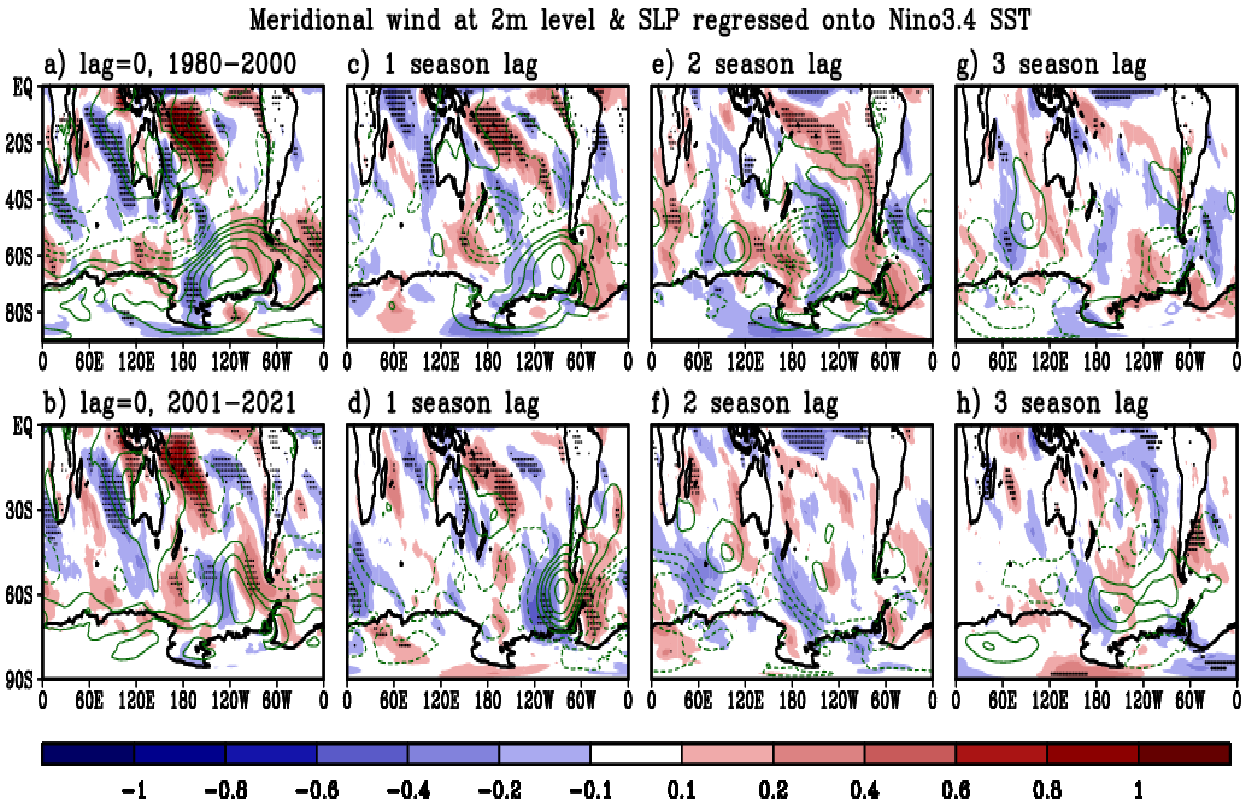

Figure 7. Same as Figure 5 but for regressed anomalies of 2-meter level meridional flow (shaded) and sea level pressure (contoured). Time-lagged response lasts longer and the meridional flow over the Ross-Amundsen-Bellingshausen Sea reaches the maximum in the late 20th century (e), while the lagged response gets weak at the same lag in the early 21st century (f).

A more detailed depiction of the time evolution of the meridional wind anomaly regressed onto El Niño maturity is shown on a monthly time scale in Figure 8. It is apparent that during the L20 period, the poleward wind at 150-120°W reaches its maximum at a 5-7 month lag, suggesting the inflow of warmer air towards the Ross and Amundsen Sea region (Figure 8a). On the contrary, in the E21 period, the strongest poleward wind anomaly occurs at a 0-4 month lag at 135-105°W (Figure 8b), which aligns with the largest sea ice decrease found at these longitudes, as shown in Figure 5. Furthermore, the presence of equatorward wind anomalies blowing from the Antarctic land is seen at various time lags (indicated by red shading over 80-90°S). This equatorward near-surface wind carries colder Antarctic air, which might act as a katabatic wind that transports dense and cold air from the elevated Antarctic inland icesheet to the coastal area [52, 53], counteracting the sea ice decrease over the RAB Sea caused by the impact of El Niño.

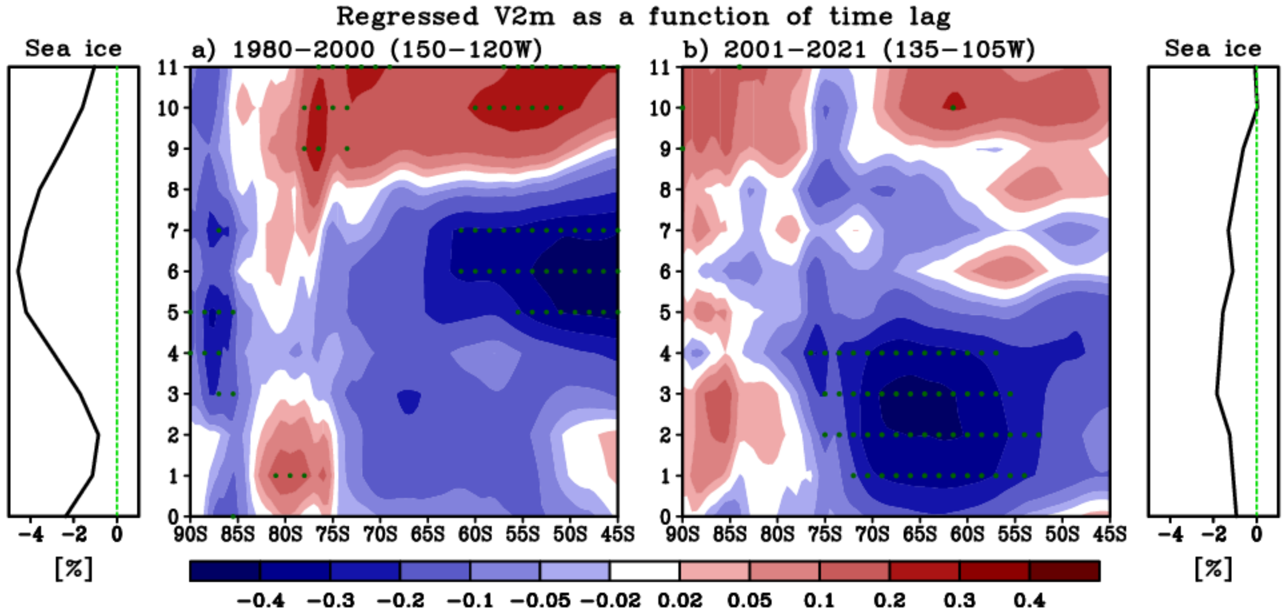

Figure 8. Shaded: Latitude (x-axis)-time_lag (y-axis) cross-section of the 2-meter level meridional wind anomalies regressed onto the boreal winter Niño3.4 SST. X-axis denotes the latitude from 90°S to 45°S and y-axis denotes the time lag ranging from 0 to 11 month. The left panel represents the result for the late 20th century while the right panel is the result for the early 21st century period. Longitudinal width for averaging the meridional winds is 150°-120°W that covers the Ross and Amundsen Sea for the late 20th century (left) and 135°-105°W that covers the Amundsen and Bellingshausen Sea for the early 21st century (right). Green stippled areas indicate that the anomalies are statistically significant at 95% confidence levels. Time series: Regressed sea ice fraction anomaly over the Ross and Amundsen Sea (left) and the Amundsen and Bellingshausen Sea (right), respectively, as a function of time lag from 0 to 11 month. X-axis denotes the regressed anomaly in percentage. The contrast is evident: during the late 20th century (left), the prevailing negative wind anomaly (poleward northly flow depicted by blue shading) is most pronounced at lags of 5-7 months, resulting in the greatest reduction in sea ice at those lags. Conversely, in the early 21st century (right), the most robust poleward northerly flow is seen at lags of 0-4 months, aligning with the highest sea ice reduction at those lags.

4.2. Lagged responses of the upper troposphere and wave activity to the mature phase of ENSO

To discuss if the time evolution of the near-surface meridional wind over the RAB Sea is linked to the development of upper-level circulation as a teleconnection response to ENSO, we examine the 300hPa level wind and geopotential height anomalies regressed onto the boreal winter Niño 3.4 SST. Figures in this section clearly explain that upper-level wind and WAF in response to ENSO is more pronounced in the L20, with their lagged response lasting longer than the E21 period. To present their spatio-temporal evolution more precisely, the results are shown with respect to monthly time lag in Figure 9. In both L20 (left) and E21 (right) periods, a clear anticyclonic (i.e., counterclockwise) circulation cell, accompanied by an increase in geopotential height, is seen in the central-eastern part of the tropical Pacific as a response to El Niño maturity (Figures 9a-l) [54]. This circulation cell remains active up to a 4-5 month lag, although it gradually weakens over time. However, while the positive anomaly in geopotential height continues in the tropical Pacific up to a 7 month lag in the L20 (Figure 9n), it is no longer evident after a 5 month lag in the E21 (Figures 9p-r, v-x), indicating a relatively stronger tropical ENSO forcing in the L20. In the extratropical region, a pattern of concatenated positive and negative geopotential height anomalies, along with corresponding circulation cells, suggests a wave train originating from the tropical Pacific [19-25]. The distribution of wave activity flux shown in Figure 10 further clarifies that the circulation/height distributions depicted in Figure 9 represent large-scale wave propagation from the tropical Pacific to the extratropics. Contours that represent the Rossby wave source in Figure 10 exhibit clearly that the tropical Pacific is a wave source more dominantly at lags of 0 and 1 season (Figures 10a-d). This wave train extends to the subpolar region, spanning the RAB and Weddell Sea. The arrangement of wave flux vectors and height anomalies in these regions in Figure 10a (L20 case) bears a resemblance to the pattern observed during an EP El Niño event, and the pattern shown in Figure 10b (E21 case) mirrors the pattern observed during a CP El Niño event, aligning with the findings of Zhang et al. [33].

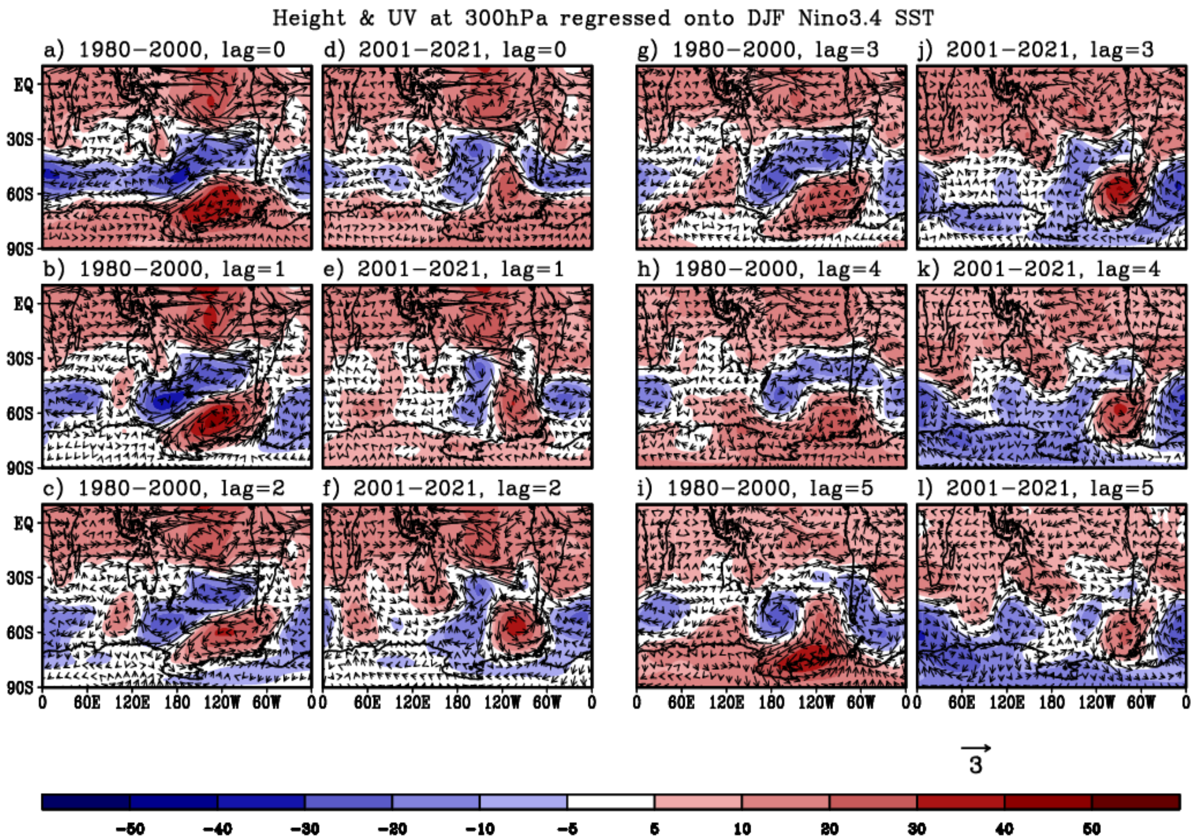

Figure 9. Distributions of 300 hPa level wind (vector) and geopotential height (shaded) anomalies regressed onto the boreal winter Niño3.4 SST. Time-lagged regression of the wind and geopotential height is conducted considering time lags of 0 to 11 month onto the boreal winter Niño3.4 SST. The first and the third column from the left represent the results for the late 20th century, and the results for the early 21st century are shown in the second and the fourth column. The northwest-southeast oriented regressed anomalies in the Pacific at lags of 0-3 months, followed by zonally oriented high/low pressure anomalies remaining active at lags of 5-7 months, is dominant in the 20th century, while the regressed anomalies weaken earlier and are no longer evident after a 5 month lag in the 21st century.

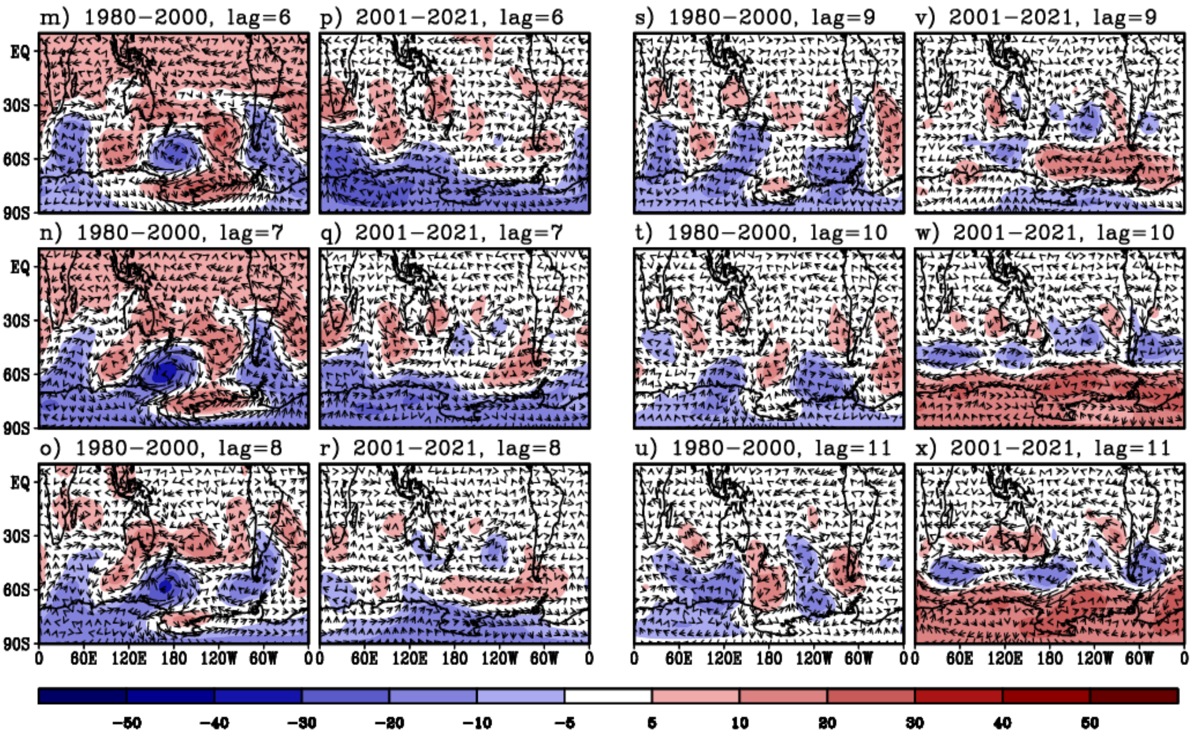

Figure 9. Continued.

Although both periods exhibit a similar spatial structure, there are some distinctions in the specific positions of geopotential height and circulation anomalies between the two periods. The circulation cell, geopotential height, and wave propagation path at 0-4 month lag during the L20 tend to be oriented northwest-southeast, resulting in the formation of a widespread anticyclonic circulation cell over the RAB Sea, and a cyclonic circulation over the Weddell Sea along the wave propagation path (Figures 9a-c, g-h, Figures 10a,c). However, the wave propagation path in the E21 appears to be more zonally oriented (Figures 9d-f, j-k, Figures 10b,d) at 0-4 month lag, and the anticyclonic circulation tends to be smaller in size than in the L20 over the Amundsen Sea, extending towards the Bellingshausen Sea (Figures 9j,k). This notable difference between the two periods leads to warmer air flowing into the Ross and the western side of the Amundsen Sea region during the L20. Conversely, the position of the warmer air inflow in the E21 shifts to the east, resulting in the area of sea ice decrease being located east of that observed in the L20, as demonstrated in Figure 5.

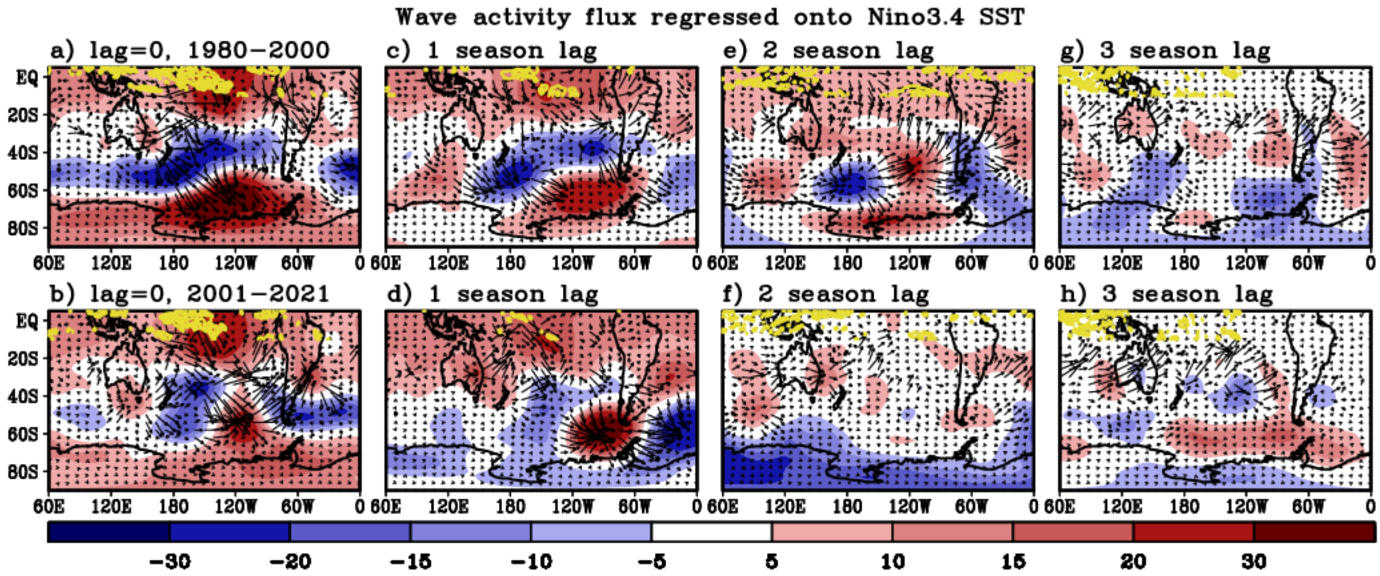

Figure 10. Distribution of 300 hPa geopotential height (shaded) and wave activity flux vectors regressed onto the boreal winter Niño3.4 SST. In each set of panels, moving from left to right, the depicted distributions are the regressed distributions considering time lags of 0, 1, 2, and 3 seasons. The upper panel displays results for the late 20th century, while the lower panel exhibits results for the early 21st century. Yellow contour lines denote the wave source region in the tropical Pacific based on the Rossby wave source calculation. A prevailing northwest-southeast aligned Rossby wave train is prominent at lags of 0 and 1 season during the 20th century (upper-panel, a and c), followed by wave flux vectors aligned more zonally at a lag of 2 seasons (e), while the wave train is notably insignificant at that lag in the 21st century (lower panel, f).

Another significant disparity in the upper-tropospheric structure between the two periods lies in the persistence of circulation cells, corresponding height anomalies and wave propagation activity across the RAB and Weddell Sea at longer time lags (approximately 5-8 months) in the L20 (Figures 9i, m-o, Figure 10e). In contrast, these anomalies substantially diminish in the E21 (Figures 9l, p-r, Figure 10f) in line with the earlier weakening of the ENSO signal in the tropics. This decadal difference may be reflected as the weakened Antarctic circumglobal wave in the E21 found in Lu et al. [55]. During the L20 period, the position of the circulation cells changes to a zonal orientation over the SO at 5-8 month lag (Figures 9i, m-o), as the strong connection with the tropical ENSO forcing at shorter time-lags gradually weakens. This shift favors a more robust meridional inflow from low-latitudes to high-latitudes at the longitudes of the Ross and Amundsen Sea, resulting in the most pronounced sea ice decrease during this time lag.

In summary, the circulation and pressure fields, and wave activity flux vectors discussed in sections 4.1 and 4.2 make it evident that the sea ice decrease over the RAB, peaking two seasons after El Niño matures, is attributed to the increased meridional poleward flow resulting from well-structured high/low pressure systems in zonal direction and accompanying wave activity across the RAB during that time lag. This distinct pattern is apparently significant in the L20, connected well with the L20’s ENSO, but the significance of this pattern diminishes in the E21, indicating a weaker role of ENSO that occurred in the E21.

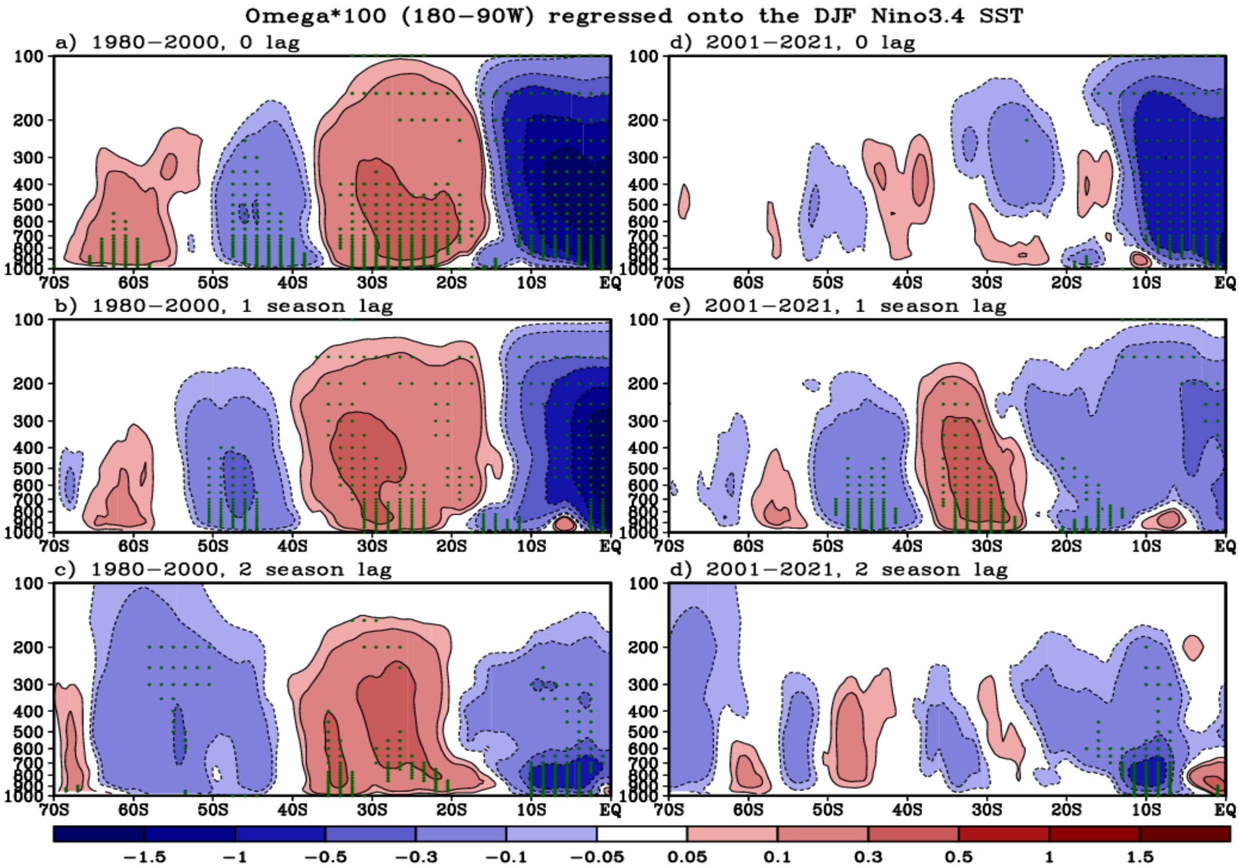

Figure 11. Latitude-height cross-section of the vertical pressure velocity at each pressure level regressed onto the boreal winter Niño3.4 SST. Longitudinal width for averaging is 180°-90°W that encompasses the central to eastern Pacific. The left panel is the result for time lag of 0 to 2 seasons in the late 20th century while the right panel represents the result for the early 21st century period. Green stippled areas indicate that the anomalies are statistically significant at 95% confidence levels. Vertical circulation cells spanning from the tropical Pacific to Antarctica is well-structured during the late 20th century (left), while the vertical structure is less well-organized in the early 21st century.

4.3. Lagged responses of the Hadley/Ferrell cell in the Pacific sector to the mature phase of ENSO

A more pronounced extra-tropical reaction to ENSO in the L20 is also detected throughout the entire vertical extent of the troposphere regarding the vertical circulation patterns of the Hadley and Ferrell cells over the Pacific region. The latitude-height cross-section of vertical pressure velocity displayed in Figure 11, focusing on time lags of 0 to 2 seasons, illustrates the well-structured vertical air circulation cells spanning from the tropical Pacific region to Antarctica during the L20 period (Figures 11a-c). In contrast, this arrangement is not as clearly established during the E21 period (Figures 11d-f). The strength of the vertical motion associated with the Hadley cell is notably greater in the L20, indicating a more potent influence from ENSO compared to the E21. This distinction enables a more robust and enduring extratropical response that significantly impacts the sea ice over the RAB region in the L20 period.

4.4. Discussion about the cause of decadal changes in ENSO type and intensity

Although this study provides valuable insights, there are several other significant questions that require further discussion. For instance, the relative contribution of ENSO type and intensity to changes in the response of the Antarctic sea ice needs investigation. However, accurately distinguishing the impact of changing ENSO type and intensity using limited ENSO observations poses a challenge. One viable approach to achieve this separation involves conducting model experiments, integrating various ENSO conditions (such as EP, CP, strong, and weak ENSO) into the model to examine the remote response in the Antarctic region to each condition. This methodology represents a key aspect of our forthcoming study, elaborated upon in the subsequent Section 4.5.

Cause of decadal changes in ENSO is also a critical question that needs to be answered. Earlier studies have indicated that ENSO variability tends to diminish during the positive phase of the Atlantic Multi-decadal Oscillation (AMO), and strengthen during its negative phase [56-58]. The AMO index is primarily in negative phase in the L20 and has shifted to a positive phase since then [59]. This decadal transition in the AMO aligns well with the decadal shift in ENSO intensity observed in our study, moving from a strong ENSO to a weak one. In terms of the underlying dynamics, Kang et al. [56] identified that the westward shift and weakening of the ENSO zonal wind stress anomalies in the equatorial central Pacific during the positive phase of the AMO contribute to the reduction in ENSO amplitude. This alteration in pattern is also connected with more frequent occurrence of CP El Niño. Expanding on this pattern shift, Chung and Li [58] illustrate a shift in the equatorial Pacific around 1988/99, characterized by strengthened trades and cooling over the eastern Pacific, providing a more favorable condition for CP El Niño occurrences in the E21 period.

4.5. Potential model experiments in the upcoming research

The majority of the conclusions drawn in this study are based on observational evidence. To strengthen these findings, it would be valuable to conduct model experiments to explore the complex relationship between ENSO and Antarctic sea ice. The next study will primarily focus on a series of model experiments, utilizing both a simple dry version of the atmospheric general circulation model applied in Zhang et al., Lim et al., and Kim et al. [33, 60, 61] and the state-of-the-art global coupled model. While the former offers valuable insights into the response of large-scale extratropical waves to tropical heat forcing, it has limitations when it comes to fully understanding the sea ice response. Experiments using the latter model, which can involve year-long simulations with a model forced by different types and intensities of ENSO, would be beneficial in capturing the corresponding sea ice response as a function of monthly time lags. Performing idealized runs by prescribing tropical Pacific SST and incorporating different intensities and types of ENSO could provide valuable insights. This approach would allow us to assess the sensitivity of the Antarctic teleconnection and sea ice response to individual changes in ENSO intensity and type. One thing we need to acknowledge is a potential deficiency of the model in representing observed response to different ENSO characteristics. Preliminary tests have indicated that the model bias affects the Antarctic remote response to ENSO and slightly underestimates the observed variations in responses to different ENSO characteristics (not shown). Therefore, while model experiments can support observational evidence, they require careful consideration.

5. Conclusions

In this study, we examined the time-lagged response of the Sea Ice Fraction (SIF) interannual anomalies over the RAB Sea in relation to the evolving ENSO over the last four decades. Regarding the decadal differences of ENSO, the composite of Niño 3.4 SST anomalies for ENSO events is shown to be ~34% larger in amplitude for El Niño (and ~53% larger for La Niña) in the L20 period compared to the E21 period. It is also observed that EP type ENSO events tend to occur more frequently in the L20, while CP type ENSO is more dominant in the E21.

Higher time-lagged correlations between ENSO and SST over the RAB Sea in the L20, than in the E21, indicates that the stronger ENSO events during the L20 period provide a better explanation for the SST variations over the RAB compared to the E21 period. Due to this difference in ENSO intensity, the response of SIF decrease and SST increase over the Ross and Amundsen Sea regions to El Niño is most prominent at shorter time-lags (e.g., 0-4 months) and weakens in E21, whereas the sea ice continues to decline during L20, reaching its peak at a two-season lag (e.g., 5-7 months).

Furthermore, the lagged response of the atmospheric circulation to ENSO shows a decadal distinction in the teleconnection and wave propagation patterns. The regressed maps consistently indicate an earlier weakening of the tropical-Antarctic remote teleconnection and a weaker AD pattern in the E21, suggesting a potential association between this decadal change in the AD and the decadal change in ENSO intensity. The wave propagation pattern during the L20 period generates a zonally oriented system of high- and low-pressure areas approximately two seasons after El Niño maturity, which helps to strengthen the poleward meridional flow. This flow plays a key role in enhancing the sea ice melt in the RAB Sea with a lag of two seasons. However, in the E21, this wave propagation is no longer evident at the same time lag, and the region of sea ice melt is determined by the circulation, which shifts eastward from the pattern seen in the L20.

It is important to mention that the eastward shift of the region of decreasing sea ice in the E21 seems contradictory to Zhang et al. [33]'s conclusion, which suggests a westward shift of the sea ice melt region by about 20° during CP El Niño. However, Zhang et al. [33]'s conclusion was specific to the Austral spring (September to November) during El Niño development years, whereas our study focuses on sea ice changes from June to August, which corresponds to the peak response after El Niño maturity [26]. This implies that the connection between El Niño and sea ice in the RAB Sea region can vary depending on the season and the phase of El Niño [26, 33].

Author Contributions: Conceptualization, Y.L., and D.W.; methodology, Y.L.; software, Y.L.; validation, Y.L., D.W., K.K., and J.L.; formal analysis, Y.L. and K.K.; writing-original draft preparation, Y.L.; writing-review and editing, Y.L., D.W., K.K., and J.L.; visualization, Y.L.; supervision, D.W.; project administration, D.W.; funding acquisition, D.W. All authors have read and agreed to the published version of the manuscript.

Funding: This research was supported by NASA Sun-Climate research fund to Goddard Space Flight Center, award number 509496.02.03.01.17.04.

Data Availability Statement: Data supporting reported results are available at https://gmao.gsfc.nasa.gov/gmaoftp/ylim/Decadal_change_Antarctic/.

Acknowledgments: The Merged Hadley-NOAA/OI SST dataset is downloaded from https://gdex.ucar.edu/dataset/158_asphilli.html. MERRA-2 data are downloaded from NASA's EarthData website https://disc.gsfc.nasa.gov/datasets/. The sea ice data from the NSIDC is downloaded from https://nsidc.org/data/G10010.

Conflicts of Interest: The authors declare no conflicts of interest.

Appendix A

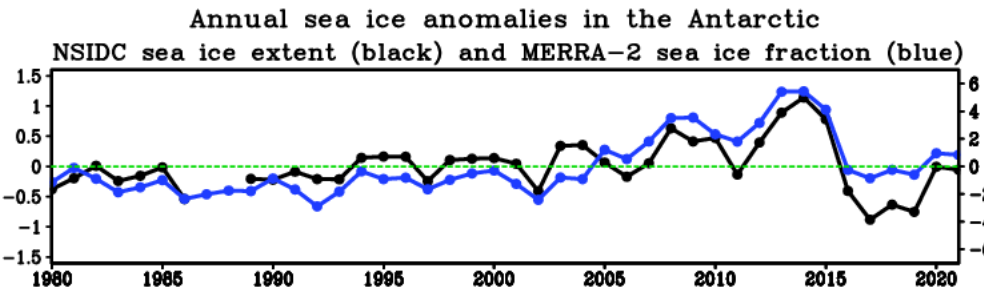

Figure A1. Time series of annual mean NSIDC sea ice extent anomaly (million km^2) (black) and MERRA-2 sea ice fraction anomaly (blue) averaged over the entire Southern Hemisphere.

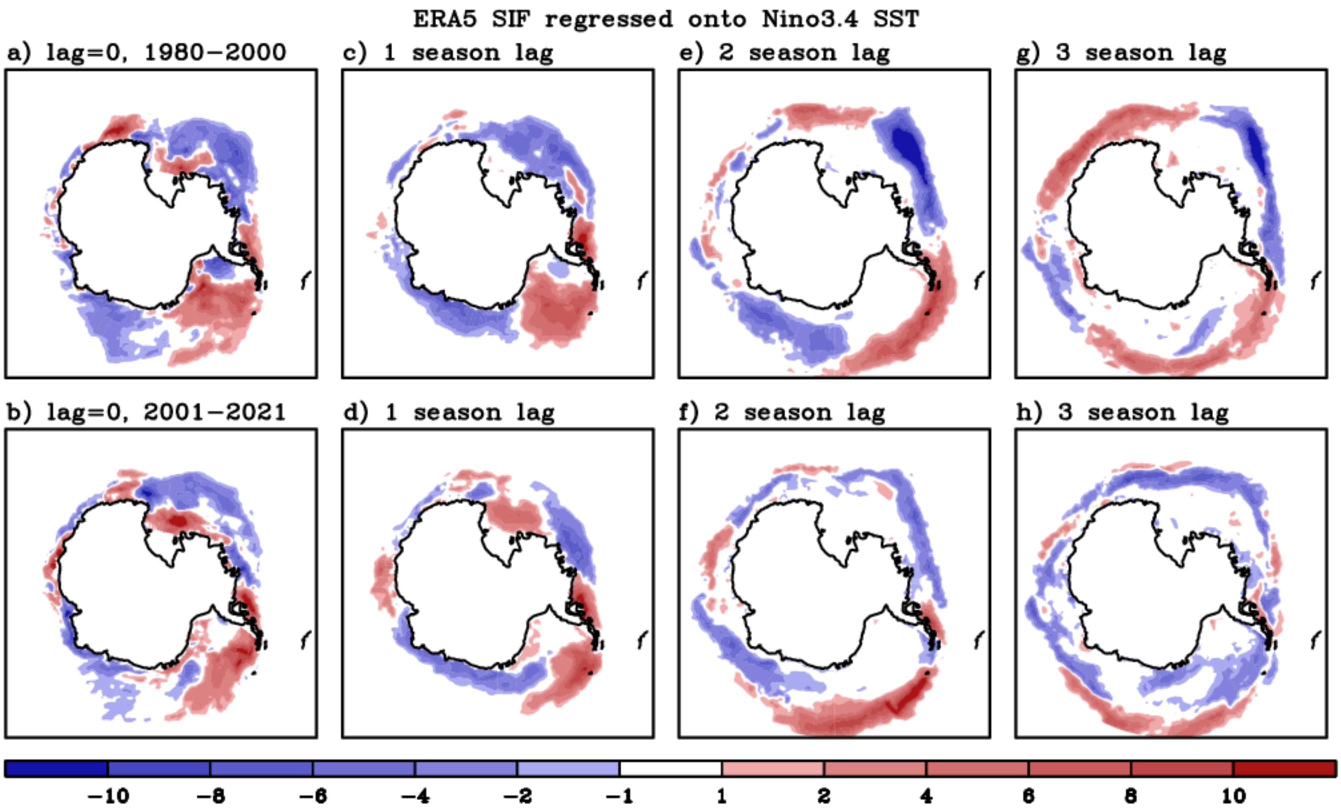

Figure A2. Distribution of ERA5 sea ice fraction (shaded) anomaly regressed onto the boreal winter Niño3.4 SST. Each panel from the left to the right represents the regressed distributions for 0, 1, 2, and 3 season lag. Results for the late 20th century are shown on the upper panel while the lower panel corresponds to the result for the early 21st century.

References

1. Carleton, A. M. Antarctic sea-ice relationship with indices of the atmospheric circulation of the Southern Hemisphere. *Clim. Dyn.*, **1989**, *3*, 207-220. https://doi.org/10.1007/BF01058236.
2. Gloersen, P. Modulation of hemispheric sea-ice cover by ENSO events. *Nature*, **1995**, *373*, 503-506. https://doi.org/10.1038/373503a0.
3. Simmonds, I.; Jacka, T. H. Relationship between the interannual variability of Antarctic sea ice and the Southern Oscillation. *J. Clim.*, **1995**, *8*, 637-647. https://doi.org/10.1175/1520-0442(1995)008<0637:RBTIVO>2.0.CO;2.
4. Ledley, T. S.; Huang, Z. A possible ENSO signal in the Ross Sea. *Geophys. Res. Lett.*, **1997**, *24*, 3253-3256. https://doi.org/10.1029/97GL03315.
5. Yuan, X.; Martinson, D. G. Antarctic sea ice extent variability and its global connectivity. *J. Clim.*, **2000**, *13*, 1697-1717. https://doi.org/10.1175/1520-0442(2000)013<1697:ASIEVA>2.0.CO;2.
6. Yuan, X.; Li, C. H. Climate modes in southern high latitudes and their impacts on Antarctic sea ice. *J. Geophys. Res.*, **2008**, *113(C6)*. https://doi.org/10.1029/2006jc004067.
7. Simpkins, G. R.; Ciastro, L. M.; Thompson, D. W. J.; England, M. H. Seasonal relationships between large-scale climate variability and Antarctic sea ice concentration. *J. Clim.*, **2012**, *25*, 5451-5469. https://doi.org/10.1175/JCLI-D-11-00367.1.
8. Kwok, R.; Comiso, J. C.; Lee, T.; Holland, P. R. Linked trends in the south Pacific sea ice edge and southern oscillation index. *Geophys. Res. Lett.*, **2016**, *43*, 10295-10302. https://doi.org/10.1002/2016gl070655.
9. Mo, K. C.; Ghil, M. Statistics and dynamics of persistent anomalies. *J Atmos. Sci.*, **1987**, *44*, 877-901. https://doi.org/10.1175/1520-0469(1987)044<0877:SADOPA>2.0.CO;2.
10. Kidson, J. W.; Interannual variations in the Southern Hemisphere circulation. *J. Clim.*, **1988**, *1*, 1177-1198.

https://doi.org/10.1175/1520-0442(1988)001<1177:IVITSH>2.0.CO;2.

11. Karoly, D. J. Southern Hemisphere circulation features associated with El Niño-Southern Oscillation events. *J. Clim.*, **1989**, *2*, 1239-1251. https://doi.org/10.1175/1520-0442(1989)002<1239:SHCFAW>2.0.CO;2.
12. Mo, K. C.; Higgins, R. W. The Pacific-South American modes and tropical convection during the Southern Hemisphere winter. *Mon. Wea. Rev.*, **1998**, *126*, 1581-1596. https://doi.org/10.1175/1520-0493(1998)126<1581:TPSAMA>2.0.CO;2.
13. Carleton, A, M, Atmospheric teleconnections involving the Southern Ocean. *J Geophy Res – Ocean*, **2003**, *108*, C4 8080. https://doi.org/10.1029/2000JC000379.
14. Bodart, J. A.; Bingham, R. J. The impact of the extreme 2015-2016 El Niño on the mass balance of the Antarctic ice sheet. *Geophys. Res. Lett.*, **2019**, *46*, 13862-13871. https://doi.org/10.1029/2019GL084466.
15. Issacs, F. E.; Renwick, J. A.; Mackintosh, A. N.; Dadic, R. ENSO modulates summer and autumn sea ice variability around Dronning Maud Land, Antarctica. *J. Geophys. Res. - Atmos.*, **2021**, *126*, e2020JD033140. https://doi.org/10.1029/2020JD033140.
16. Zhang, Y.; Wallace, J. M.; Battisti, D. S. ENSO-like interdecadal variability: 1900-93. *J. Clim.*, **1997**, *10*, 1004-1020. https://doi.org/10.1175/1520-0442(1997)010<1004:ELIV>2.0.CO;2.
17. Garreaud, R.; Battisti, D. S. Interannual (ENSO) and interdecadal variability in the Southern Hemisphere tropospheric circulation. *J. Clim.*, **1999**, *12*, 2113-2123. https://doi.org/10.1175/1520-0442(1999)012<2113:IEAIEL>2.0.CO;2.
18. Yuan, X. ENSO-related impacts on Antarctic sea ice: a synthesis of phenomenon and mechanisms. *Antarctic Sci.*, **2004**, *16(4)*, 415-425. https://doi.org/10.1017/S0954102004002238.
19. Kalnay, E.; Mo, K. C.; Paegle, J. Large-amplitude, short-scale stationary Rossby waves in the Southern Hemisphere: Observations and mechanistic experiments to determine their origin. *J. Atmos. Sci.*, **1986**, *43*, 252-275.
20. Berbery, E. H.; Nogues-Paegle, J.; Horel, J. D. Wavelike Southern Hemisphere extratropical teleconnections. *J. Atmos. Sci.*, **1992**, *49*, 155-177. https://doi.org/10.1175/1520-0469(1992)049<0155:WSHET>2.0.CO;2.
21. Grimm, A. M.; Silva-Dias, P. L. Analysis of tropical-extratropical interactions with influence functions of a barotropic model. *J. Atmos. Sci.*, **1995**, *52*, 3538-3555. https://doi.org/10.1175/1520-0469(1995)052<3538:AOTIWI>2.0.CO;2.
22. Renwick, J. A.; Revell, M. J. Blocking over the South Pacific and Rossby wave propagation. *Mon. Wea. Rev.*, **1999**, *127*, 2233-2247. https://doi.org/ 10.1175/1520-0493(1999)127<2233:BOTSPA>2.0.CO;2
23. Mo, K. C.; Paegle, J. N.. The Pacific-South American mode and their downstream effects. *Int. J. Climatol*. **2001**, *21(10)*, 1211-1229. https://doi.org/10.1002/joc.685.
24. Irving, D.; Simmonds, I. A new method for identifying the Pacific-South American pattern and its influence on regional climate variability. *J. Clim.*, **2016**, *29*, 6109-6125. https://doi.org/10.1175/JCLI-D-15-0843.1.
25. Lou, J.; O'Kane, T. J.; Holbrook, N. J. Linking the atmospheric Pacific-South American mode with oceaninc variability and predictability. *Commun. Earth Environ.*, **2021**, *2*, 223. https://doi.org/10.1038/s43247-021-00295-4.
26. Dou, J.; Zhang, R. Weakened relationship between ENSO and Antarctic sea ice in recent decades. *Clim. Dyn.*, **2023**, *60*, 1313-1327. https://doi.org/10.1007/s00382-022-06364-4.
27. Cai, W.; Santoso, A.; Collins, M.; Dewitte, B.; Karamperidou, C.; Kug, J.-S.; et al. Changing El Niño-Southern Oscillation in a warming climate. *Nat. Rev. Earth Environ.*, **2021**, *2*, 628-644. https://doi.org/10.1038/s43017-021-00199-z.
28. Hu, K.; Huang, G.; Huang, P.; Kosaka, Y., Xie, S.-P. Intensification of El Niño-induced atmospheric anomalies under greenhouse warming. *Nat. Geosci.*, **2021**, *14*, 377-382. https://doi.org/10.1038/s41561-021-00730-3.
29. Wang, Y.; Huang, G.; Hu, K.; Tao, W.; Gong, H.; Yang, K.; Tang, H. Understanding the eastward shift and intensification of the ENSO teleconnection over South Pacific and Antarctica under greenhouse warming. *Front. Earth Sci.*, **2022**, *10*. https://doi.org/10.3389/feart.2022.916624.
30. Fogt, R. L.; Bromwich, D. H. Decadal variability of the ENSO teleconnection to the high-latitude South Pacific governed by coupling with the Southern Annular Mode. *J. Clim.*, **2006**, *19*, 979-997. https://doi.org/10.1175/JCLI3671.1.

31. Yu, J.-Y.; Paek H.; Saltzman, E. S.; Lee, T. The early 1990s change in ENSO-PSA-SAM relationships and its impact on Southern Hemisphere change. *J. Clim*., **2015**, *28*, 9393-9408. https://doi.org/10.1175/JCLI-D-15-0335.1.
32. Yeo, S.; Kim, K.-Y. Decadal changes in the Southern Hemisphere sea surface temperature in association with El Niño-Southern Oscillation and Southern Annular Mode. *Clim. Dyn*., **2015**, *45*, 3227-3242. https://doi.org/10.1007/s00382-015-2535-z.
33. Zhang, C.; Li, T.; Li, S. Impacts of CP and EP El Niño events on the Antarctic sea ice in Austral spring. *J. Clim*., **2021**, *34*, 9327-9348. https://doi.org/10.1175/JCLI-D-21-0002.1.
34. Harangozo, S. The relationship of Pacific deep tropical convection to the winter and springtime extratropical atmospheric circulation of the South Pacific in El Niño events. *Geophys. Res. Lett*., **2004**, *31:L05206*. https://doi.org/10.1029/2003GL018667.
35. Lachlan-Cope, T.; Connolley W. Teleconnections between the tropical Pacific and the Amundsen-Bellingshausen Sea: role of the El Niño-Southern Oscillation. *J. Geophys. Res*., **2006**, *111:D23101*. https://doi.org/10.1029/2005JD006386.
36. Chen, X.; Li, S.; Zhang, C. Distinct impacts of two kinds of El Niño on precipitation over the Antarctic Peninsula and West Antarctica in austral spring. *Atmos. Ocean. Sci. Let*., **2023**, *16*, 100387. https://doi.org/10.1016/j.aosl.2023.100387.
37. Hartmann, D. L.; Lo, F. Wave-driven zonal flow vacillation in the Southern Hemisphere. *J. Atmos. Sci*., **1998**, *55*, 1303-1315. https://doi.org/10.1175/1520-0469(1998)055<1303:WDZFVI>2.0.CO;2.
38. Thompson, D. W. J.; Wallace, J. M. Annular modes in the extratropical circulation. Part I: Month-to-month variability. *J. Clim*., **2000**, *13*, 1000-1016. https://doi.org/10.1175/1520-0442(2000)013<1000:AMITEC>2.0.CO;2.
39. Song, H.-J.; Choi, E.; Lim, G.-H.; Kim, Y. H.; Kug, J.-S.; Yeh, S.-W. The central Pacific as the export region of the El Niño-Southern Oscillation sea surface temperature anomaly to Antarctic sea ice. *J. Geophys. Res. – Atmos*., **2011**, *116*, D21113. https://doi.org/10.1029/2011JD015645.
40. Hurrell, J. W.; Hack, J. J.; Shea, D.; Caron, J. M.; Rosinski, J. A new sea surface temperature and sea ice boundary dataset for the Community Atmosphere Model. *J. Clim*., **2008**, *21*, 5145-5153. https://doi.org/10.1175/2008JCLI2292.1.
41. Gelaro, R.; et al. The Modern-Era Retrospective Analysis for Research and Applications, Version 2 (MERRA-2). *J. Clim*., **2017**, *30*, 5419-5454. https://doi.org/10.1175/JCLI-D-16-0758.1.
42. GMAO 2015a MERRA-2 instM_3d_asm_Np, 3d, monthly mean, instantaneous, pressure-level, assimilation, assimilated meteorological fields, version5.12.4, Global Modeling and Assimilation Office, Goddard Space Flight Center Distributed Active Archive Center (GSFC DAAC), accessed Apr 2023.
43. GMAO 2015b MERRA-2 tavgM_2d_slv_Nx, 2d, monthly mean, time-averaged, single level, assimilation, single-level diagnostics, version5.12.4, Global Modeling and Assimilation Office, Goddard Space Flight Center Distributed Active Archive Center (GSFC DAAC), accessed Apr 2023.
44. GMAO 2015c MERRA-2 tavgM_2d_rad_Nx, 2d, monthly mean, time-averaged, single level, assimilation, radiation diagnostics, version5.12.4, Global Modeling and Assimilation Office, Goddard Space Flight Center Distributed Active Archive Center (GSFC DAAC), accessed Apr 2023.
45. Walsh, J. E.; Chapman, W. L.; Fetterer, F.; Steward, J. S. Gridded monthly sea ice extent and concentration, 1850 onward, version 2. National Snow and Ice Data Center (NSIDC), 2019, Available at https://doi.org/10.7265/jj4s-tq79, accessed Apr2023.
46. Hersbach, H.; Bell, B.; Berrisford, P.; Hirahara, S. et al. The ERA5 global reanalysis. *Quart. J. Roya. Meteor. Soc*., **2020**, *146*, 1999-2049. https://doi.org/10.1002/qj.3803.
47. Li, S.; Cai, W.; Wu, L. Weakened Antarctic Dipole under global warming in CMIP6 models. *Geophys. Res. Lett*., **2021**, *48*, e2021GL094863. https://doi.org/10.1029/2021GL094863.
48. Takaya, K.; Nakamura, H. A formulation of a phase-independent wave-activity flux for stationary and migratory quasigeostrophic eddies on a zonally varying basic flow. *J. Atmos. Sci*., **2001**, *608-627*. https://doi.org/10.1175/1520-0469(2001)058<0608:AFOAPI>2.0.CO;2.
49. Plumb, R. A. On the three-dimensional propagation of stationary waves. *J. Atmos. Sci*., **1985**, *42*, 217-229.

https://doi.org/10.1175/1520-0469(1985)042<0217:OTTDPO>2.0.CO;2.

50. Sardeshmukh, P. D.; Hoskins, B. J. The generation of global rotational flow by steady idealized tropical divergence. *J. Atmos. Sci.*, **1988**, *1228-1251*. https://doi.org/10.1175/1520-0469(1988)045<1228:TG0GRF>2.0.CO;2.
51. Jakovlev, A. R.; Smyshlyaev, S. P.; Galin, V. Y. Interannual variability and trends in sea surface temperature, lower and middle atmosphere temperature at different latitudes for 1980-2019. *Atmosphere*, **2021**, *12*, 454. https://doi.org/10.3390/atmos12040454.
52. Bromwich, D. H.; Du, Y. Numerical simulation of winter katabatic winds from West Antarctica crossing Siple Coast and the Ross Ice Shelf. *Mon. Wea. Rev.*, **1994**, *122*, 1417-1435. https://doi.org/10.1175/1520-0493(1994)122<1417:NSOWKW>2.0.CO;2.
53. Parish, T. R.; Cassano, J. J. Diagnosis of the katabatic wind influence on the wintertime Antarctic surface wind field from numerical simulations. *Mon. Wea. Rev.*, **2003**, *131*, 1128-1139. https://doi.org/10.1175/1520-0493(2003)131<1128:DOTKWI>2.0.CO;2.
54. DeWeaver, E.; Nigam, S. Linearity in ENSO's atmospheric response. *J. Clim.*, **2002**, *15*, 2446-2461. https://doi.org/10.1175/1520-0442(2002)015<2446:LIESAR>2.0.CO;2.
55. Lu, Z.; Zhao, T.; Zhou, W.; Zhao, H. Interdecadal variation of the Antarctic circumpolar wave based on the 20CRV3 dataset. *Atmosphere*, **2022**, *13*, 736. https://doi.org/10.3390/atmos13050736.
56. Kang, I. S.; No, H. H.; Kucharski, F. ENSO amplitude modulation associated with the mean SST changes in the tropical central Pacific induced by Atlantic Multidecadal Oscillation. *J. Clim.*, **2014**, *27*, 7911-7920. https://doi.org/10.1175/JCLI-D-14-00018.1.
57. Xiang, B. Q.; Wang, B.; Li, T. 2013 A new paradigm for the predominance of standing central Pacific warming after the late 1990s. *Clim. Dyn.*, **2013**, *41*, 327-340. https://doi.org/10.1007/s00382-012-1427-8.
58. Chung, P. H.; Li, T. Interdecadal relationship between the mean state and El Niño types. *J. Clim.*, **2013**, *26*, 361-379. https://doi.org/10.1175/JCLI-D-12-00106.1.
59. The state of the ocean climate available online: https://stateoftheocean.osmc.noaa.gov/atm/amo.php.
60. Lim, Y.-K.; Schubert, S. D.; Chang, Y.; Wang, H. The boreal winter El Niño precipitation response over North America: Insights into why January is more difficult to predict than February. *J. Clim.*, **2020**, *33*, 8651-8670. https://doi.org/10.1175/JCLI-D-19-0841.1.
61. Kim, J.; Kang, D.; Lee, M.-I.; Jin, E. K.; Kug, J.-S.; Lee, W. S. Remote influences of ENSO and IOD on the interannual variability of the West Antarctic sea ice. *J. Geophys. Res. – Atmos.*, **2023**, *128*, e2022JD038313. https://doi.org/10.1029/2022JD038313.